Engineering Failure Analysis 148 (2023) 107203

Contents lists available at ScienceDirect

Engineering Failure Analysis

journal homepage: www.elsevier.com/locate/engfailanal

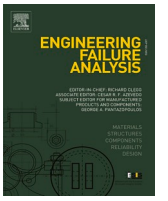

Transient dynamics of a full wheel rail set passing a weld irregularity at high speed

X. Liu [a,d,*], C. Liu [a,d], W. Wu [a], J.Z. Liu [b], S.C. Sun [b], Y.G. Wei [c]

[a] LNM, Institute of Mechanics, Chinese Academy of Sciences, Beijing 100190, China
[b] China Academy of Railway Sciences, Beijing 100844, China
[c] Peiking University, Beijing 100871, China
[d] School of Engineering Science, UCAS, Beijing 100049, China

ARTICLE INFO

Keywords:
Weld irregularity
Axle box acceleration
Finite element analysis
Safety limit

ABSTRACT

Compared to tracking the contact force, the monitoring of axle box acceleration (*ABA*) is an effective way to determine the operation status of a high–speed train passing a weld. In this study, we propose a finite element model for studying the dynamic response of a full wheelset passing weld irregularities at high speed. Simulations provide detailed dynamic information during the pass, such as the peak of the contact force and the history of acceleration. With these simulation results, we propose a standard safety limit for the running speed: a running speed boundary as a function of defect size. Additionally, rail weld defect grinding standards should depend on the running speeds.

1. Introduction

A Continuous Welded Rail (CWR) can reduce the number of joint connections of a rail. Thus, using this technique ensures the integrity of the rail [1]. Corrugation at a joint appears due to the material differences between the welding and the base [2], the thermal distortion during the welding process [3], and the welding quality produced by operators [4]. The resulting irregularities on the joint surface of a CWR, seriously affect the safety of a train [5].

Defects on a track may induce different types of engineering failure due to its size [6,7]. The components of irregularities with a longer length scale than the wheel radius or the sleeper span (0.5–0.6 m) will damage the ballast bed, whereas the components with a shorter length scale will damage the railhead and rail [6]. The weld defect normally has a shorter size, and with the increase of running speed, damage by weld defect on the railhead and rail will be worse.

The wheel–rail dynamic response of a joint has been studied using contact mechanics. Kalker et al. [8] introduced the Boundary Element Method (BEM) to numerically solve rolling contact problems under three-dimensional conditions, and proposed the linear creep theory for wheel–rail contact. However, the Kalker theory is mostly used for steady–state rolling. Zhai et al. [9] established vehicle-track coupling dynamics to study wheel–rail response at a weld so that the rail dynamic response could be obtained with an acceptable computational cost. Steenbergen et al. [10] also established a wheel-rail dynamic model. They proposed a correlation formula between the weld geometry and the extreme value of wheel–rail force, and they further used the model to evaluate the welding quality. The vehicle-rail dynamic model based on a *Timoshenko* beam could further reduce the computational cost [11]. They studied the variation of the wheel–rail contact force as the vehicle system passed the weld, and concluded that factors, such as the rail

* Corresponding author at: LNM, Institute of Mechanics, Chinese Academy of Sciences, Beijing 100190, China.
E-mail address: xiaomingliu@imech.ac.cn (X. Liu).

https://doi.org/10.1016/j.engfailanal.2023.107203
Received 7 December 2022; Received in revised form 22 February 2023; Accepted 15 March 2023
Available online 20 March 2023

equivalent mass, sprung mass, and stiffness of the ballast, had different effects on the contact forces. In the above studies, strong assumptions are used for reducing the computational cost by using BEM [8], rigid-flexible coupling [9], and the beam assumption in the contact mechanics for studying wheel–rail rolling contact. These assumptions pose difficulties in proving a transient response for the wheel-rail interaction.

However, the Finite Element Method (FEM) can provide detailed information for the transient problems of a wheel–rail rolling response. The pioneering study of the frictional rolling of wheel–rail contact was proposed by Zhao and Li [12] using explicit FEM simulation. In their study, the contact area evolution, pressure and shear stress distributions, and micro-slip distribution were compared using the software program CONTACT [8], the comparison showed high accuracy in static frictional rolling. The proposed model has been used to study compression-shift-rolling contact [13], velocity dependent frictional rolling [14], and non-steady-state transition from single-point to two-point contact [15].

Similar pioneering studies by Wen et al. [16,17] have been used for the study of a wheel–rail system. They [16] developed a similar explicit FEM to analyze the dynamic contact stress at a rail joint, and the model was further used to check the height effect of the weld joint on the dynamic response [17]. The rail-welding heat conduction process was studied using FEM [18], the developed model could be used to analyze the entire process of welding. Kabo [19] studied the size and plastic deformation of welded joints on the dynamic contact between a wheel and a rail. The results showed that the existence of a weld changed the dynamic characteristics of the orbit, and the irregularity of the orbit surface was the reason for the sharp increase in the transient contact load. An et al. [20] simulated the wheel–rail response of welded joints by using a half-mode model, and they studied the influence of the gradient of the welded joints on the wheel–rail force and axle box acceleration (*ABA*). Molodova et al. [21] used a 3D explicit FE model to simulate the change of the *ABA* as a rail passed through the weld at a running speed of 140 km/h, and the obtained results were consistent with the field test.

The wheel–rail contact force and the *ABA* are the two main parameters used to evaluate the running state of a train. In our institute [22], we used to measure the contact force by using a strain gauge on the wheel set. There are several shortcomings from our using experience. First is that, the system is complex. We have to use reliable strain gauges, because the operation environment is not friendly; and we have to make a calibration test to connect the strain with the contact force, the temperature dependent on strain may cause the calibration even worse. Second is the maintenance of the wheel set-up. The wheel is totally different with the ordinary wheel, so that the maintenance will spend a lot, both human force and economic cost. Third is the frequency limit of the strain gauge. As the train speed goes higher, the high–frequency signal such as the shock response will play a key factor to the wheel–rail system. However, the strain gauge on the wheel can not sperate the high–frequency signal from the noise. In conclude, because the *ABA* is sensitive to high–frequency response, and can be easily installed and maintained, we choose the *ABA* as a replacement of the contact force for detecting weld defect.

The maximum limit of the wheel–rail contact force is 170 kN [20] according to the safety standard for China's High–Speed Trains,

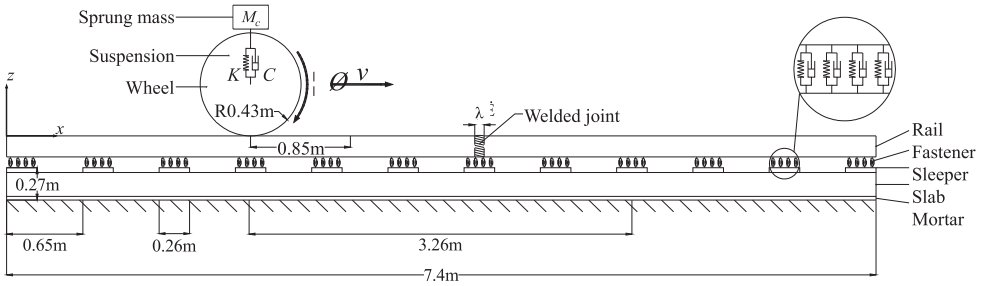

(a) The schematic diagram

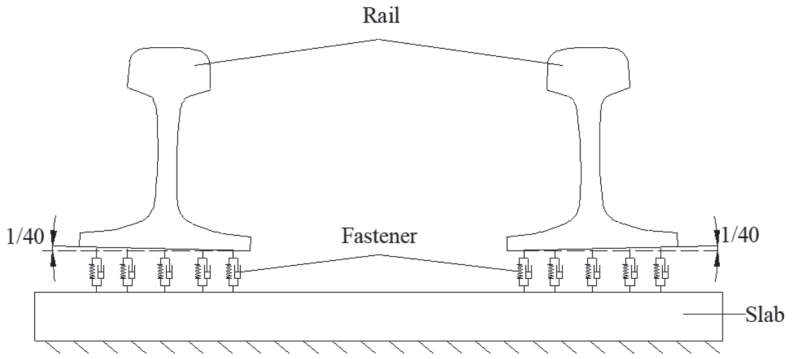

(b) Sketch of rail bottom slope

Fig. 1. The 3D wheel–rail rolling contact finite element model.

but there are no specific relations between the *ABA* and the weld geometry. Moreover, most of the previous studies considered only half-models. In the half model [20], the symmetrical boundary will add extra constraint and may cause unrealistic high–frequency response. This extra constraint will make a much bigger effect on the *ABA* than on the contact force. In this sense, half model might not be used as a quantitative model for studying the *ABA* as high–speed train passing weld. Also, presence of welded joints on both sides is much close to reality, but two side joints on the *ABA* with operating speeds from 200 km/h to 400 km/h have not yet been presented in the literature.

In this work, the rolling contact response of a full wheel–rail set is studied by using a 3D rolling FEM model. The model is verified with a previous half model study in the literature. Then, with different joint defects at two sides taken into account, we study the running speed effect (from 200 km/h to 400 km/h) on the monitored *ABA*. The *ABA* analysis is carried out in both the time and frequency domains. With the obtained correlation between the maximum *ABA* and the maximum wheel–rail force, we propose a standard safety limit for the welding depth as a function of the running speed, according to the safety limit for wheel–rail force in China.

2. FEM model

The profiles of the wheel and rail are used according to LMA and CN60 standards in China's high-speed railway system, and the rail cant is set as 1:40. The length of the rail is 7.4 m, and the wheel is initially set at a distance from the left side to eliminate the boundary effect. We choose the distance as 2.08 m as shown in Fig. 1. The suspension consists of two groups of spring dampers on both axle ends of the wheel, and each group is distributed with five spring dampers, as shown in Fig. 2. Sleepers with a width of 0.26 m are arranged on the slab. The distance between two sleepers is 0.65 m. The vertical distance between the rail and the slab is 0.01 m. The fasteners simulated by the spring and damper system are distributed in the middle of the sleeper. There are four horizontal columns and five lateral rows of fasteners on the sleeper, with a total number of 480 fasteners in the model. In our simulation, the sleeper has the same material as the slab, and the two share the nodes in the FEM model.

To reduce the computational cost, the meshing of the wheel–rail model is not uniform, as shown in Fig. 2. To keep the high accuracy of the contact simulation, a solution zone with a mesh size of 1 mm is adopted on the wheel–rail contact surface. This fine mesh size in the solution zone can ensure the contact area having enough elements for contact simulation [23] The high-density mesh is discretized over the solution zone (0.1 m to 0.3 m long) around the joint, as well as on the contact surface of the wheel. The area far away from the

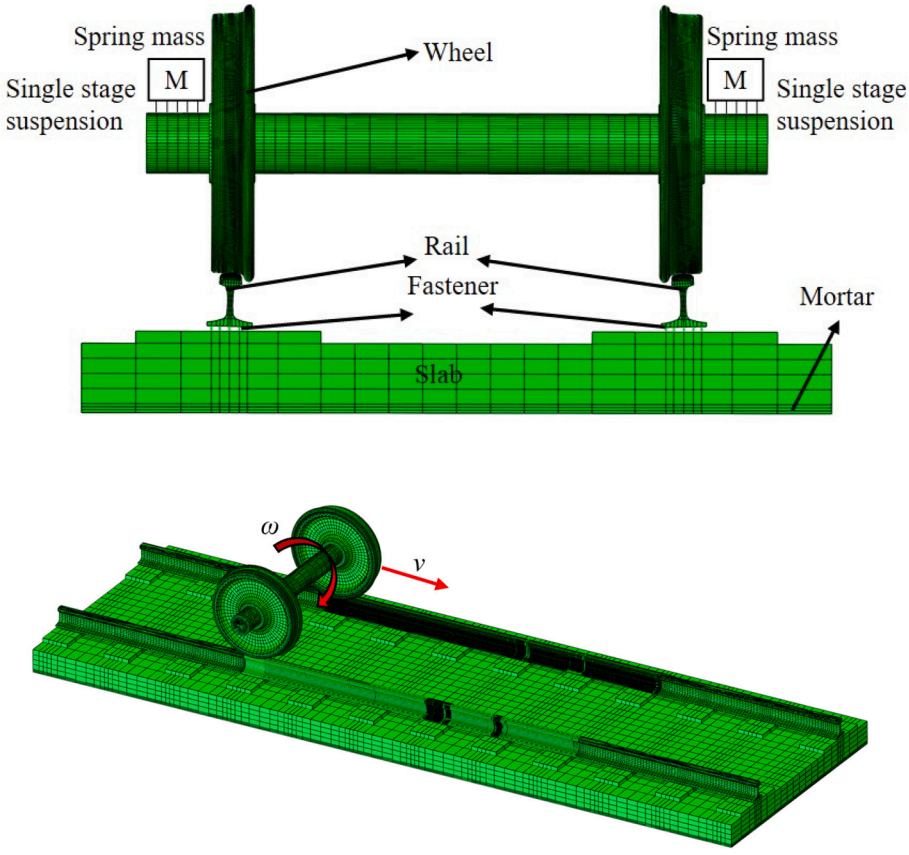

Fig. 2. The mesh of the FE model for wheel-rail wheel–rail rolling contact.

contact zone is discretized by a larger mesh. All of the rail modules are discretized by eight–node hexahedral elements. The meshing of the wheel, slab, and mortar layer is coarse, and the mesh width of the rail is mostly fine mesh with a 2 mm size. Since the wheel part is in a rotating state, the wheel is connected with a sprung mass through a distributed spring/damper unit, six–node solid elements are used at the axle and eight–node hexahedral elements are used for the rest. In our simulation, we connected the sprung mass with the center line of the axle box, so that the sprung mass will not rotate with the rotation of the axle. The total number of modeled elements is about 1.22 million, and the total number of nodes is about 1.47 million. The material parameters of each component are listed in Table. 1, we choose the system with the same parameters as in the reference [24,25], as typically used in China's high-speed system.

The geometric size of a weld is critical for studying the wheel–rail interaction response. Abe [26] investigated the weld of the Shinkansen in Japan in detail and found that the geometric shape of most welded joints was superposed by two cosine waveforms, with a long wave (1 m) and a short wave (0.1 m). Considering the fact that the wheel–rail response caused by short-wave irregularity is more severe, most studies are based on the short-wave irregularity of welded joints within the wavelength of 0.1 m to 0.5 m [27]. The weld height is another factor that affects the wheel–rail response. According to the maintenance rules for the high–speed railway in China [28], the griding limit is 0.2 mm for the weld, when the running speed is 300 km/h. The height should not exceed 0.3 mm when the running speed is 200 km/h. The weld length is mostly 0.1 m in China's high–speed rail [24,22]. Thus, in our simulation, the dimension of weld size is chosen accordingly. The geometry of the weld comes from our previous studies [24,25].

In this model, the Cartesian coordinate system *Oxyz* is used, in which the initial position of the axle center is defined as the origin *O*, and the $\times$ and *z* axes are in the longitudinal and vertical directions, respectively. The boundary conditions are applied as follows: The lateral freedom of the wheel is constrained. The rail ends are fixed. The fastenings, the slabs, and the mortar layer can only move vertically, and the bottom of the mortar layer is fixed.

The wheel–rail system is firstly employed in a simulation to reach an equilibrium state under gravity and a sprung mass load. A load with the sprung mass ($M_c \cdot g$) is applied in the suspension spring, and the spring is initially compressed with a magnitude equal to the sprung mass ($M_c \cdot g$), so that the system can reach equilibrium in a few increments. As shown in Fig. 3, the force displacement expression for the spring is:

$$F = K_f \cdot u_y - M_c \cdot g$$

Where *g* is the gravitational acceleration, u_y is the spring compression in the vertical direction, and *F* is the compression force in the vertical direction.

Then, the explicit algorithm is used for the wheel rolling. The transient rolling is simulated with the applied initial angular velocity and transitional velocity as required. The friction coefficient $f = 0.5$ is used for the wheel–rail contact.

The geometry of rail weld joints is either convex or concave. According to operational statistics, most defects are convex. The geometric shapes of the two kinds of welds can be approximated by harmonic shapes. The two-dimensional geometry of the single harmonic weld joints is shown in Fig. 4, and the profile has the expression as:

$$z = \frac{1}{2}\delta_x\left(1 - \cos\frac{2\pi x}{\lambda_x}\right)$$

Where δ_x and λ_x are the wave height and length of the weld, and *x* follows the longitudinal direction of the rail. The value of δ_x is set to be positive in the convex case, and negative in the concave case.

3. Model validation

The variation of the Axle Box Acceleration (*ABA*) as the wheels roll over smooth rails at a speed of 300 km/h is presented in Fig. 5.

Table 1
Values of parameters involved in the model.

Parameters		Values
Friction coefficient,f		0.5
Sprung mass,M_c (kg)		8000
Wheel diameter,ϕ (m)		0.86
Wheelset mass,M_w (kg)		1168
Suspension stiffness,K (kN/m)		880
Suspension damping,C (kN·s/m)		4
Fastener stiffness,K_f (MN/m)		22
Fastener damping,C_f (kN·s/m)		200
Wheel and rail materials	Young modulus,E (GPa)	205.9
	Poisson ratio,μ	0.3
	Density,ρ (kg/m^3)	7790
Slab material	Young modulus,E_s (GPa)	34.5
	Poisson ratio,μ_s	0.25
	Density,ρ_s (kg/m^3)	2500
Mortar Layer Material	Young modulus,E_m (GPa)	8
	Poisson ratio,μ_m	0.2
	Density,ρ_m (kg/m^3)	1600

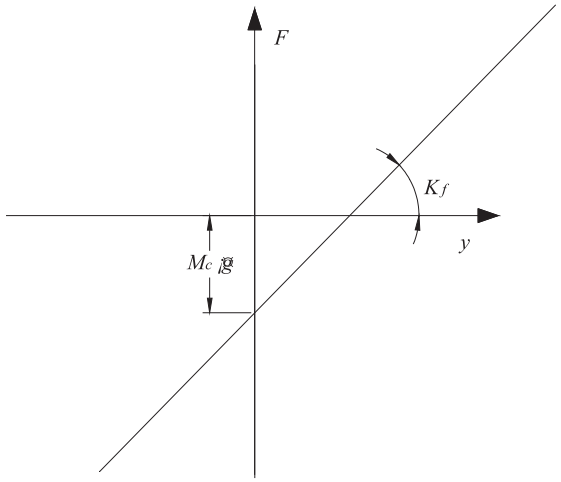

Fig. 3. Force-displacement for the suspension spring.

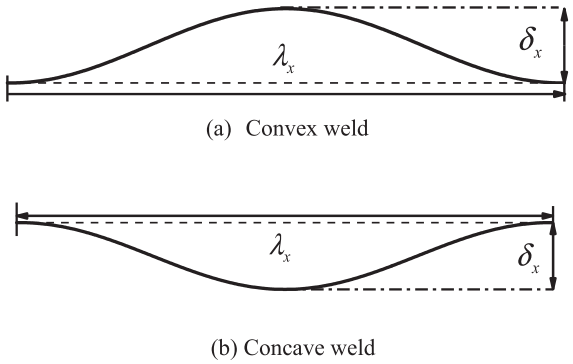

Fig. 4. Geometric shape of a weld.

It can be seen that the *ABA* oscillates fiercely at the initial moment of the wheel–rail contact. This is because of the application of the initial angular and transition velocity, as required. In the finite element simulation of the wheel–rail contact, the vibration amplitude of the *ABA* is considered to be stable within ± 10 g. From Fig. 5, it is clearly indicated that after the wheel rolls over 1 m, the *ABA* has entered an equilibrium state. In our model, the weld joint in this study is located at a position 1.8 m away from the initial location, so

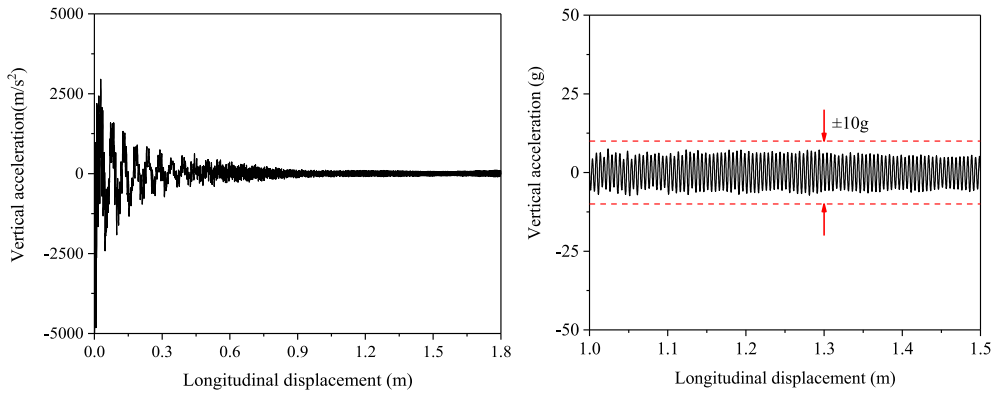

(a) Initial *ABA* as a function of displacement

(b) Stabilized *ABA* as a function of displacement

Fig. 5. *ABA* response as wheels roll over smooth rails at a speed of 300 km/h.

that the wheel–weld interaction is not affected by the initial condition.

The verification test for our model is performed by comparing the simulation with the same wheel–rail parameters as those in the literature [20] with the same convex weld defects, that is, $\lambda = 0.05$ m and $\delta = 0.2$ mm. The comparison of the simulation results is shown in Fig. 6. It is obvious that the peak value of wheel–rail contact force and the *ABA* generated by the present study is close to An's results, but the oscillation of both parameters in this work is much lower. The reason for this is that the sprung mass in our model is dispersed into ten springs, which makes the axle force more balanced. This method is much closer to the real operation situation compared to the one spring method used in the half model [20]. Moreover, this study establishes a whole wheelset model, which is more stable than the half model in the reference.

The effect of the material plasticity and the rail fastener stiffness on the wheel–rail contact response is also checked. In the actual rail, the yield strength of the welded material is 80%—90% of the base metal. For rail fasteners, the standard fastener stiffness is 22 MN/m, which will increase with the service life. Cases with stiffnesses ranging from 10 MN/m to 50 MN/m are simulated to check the effect. Also, we checked how does the plasticity of weld affect the contact force or the *ABA* by doing transient simulation. In the simulation, we set the weld as either elastic material or elastic–plastic material, and compared the results in Fig. 7.

With the transient impact, the effect of the material plasticity (yield strength set as 80% of the base material) on the peak of the contact force is less than a 1.5% deviation, and the effect of the fastener stiffness (from 10 MN/m to 50 MN/m) on the peak of the contact force is less than 1.0%. Thus, in the later simulation, the material plasticity is not considered, and the fastener stiffness is chosen as 22 MN/m.

4. Results and discussions

In Section 4.1 and 4.2, the same defects on both sides of the rail are discussed, while the unsymmetric configuration of the weld is discussed in Section 4.3.

4.1. The influence of the running speed

To analyze the influence of running speed, the running speed of the wheel is varied from 200 km/h to 400 km/h, to roll over the same convex/concave weld which has the dimension $\lambda = 0.1$ m, $\delta = \pm 0.2$ mm. Fig. 8 (a) (b) shows that the maximum value of the wheel–rail contact force increases with the increase of the running speeds for both the convex and concave welds. The maximum and minimum contact forces are given as a function of the running speed in Fig. 8 (c) (d). It can be seen from the figure that the maximum contact force has a linear relationship with the running speed for the convex weld, but it stays almost constant for the concave weld. The minimum contact force has the opposite trend.

The effect of weld on P1 and P2 forces is discussed here. Study [30] shows that P1 force is the main contribution from rail surface and subsurface damage mechanisms, and P2 force is main contribution from ballast damage mechanisms. In the present work, the weld is one type of rail surface and subsurface damage, thus we used the P1 force.

The effect of the running velocity on the *ABA* response is shown in Fig. 9. With the increase in the running speed, the vibration of the *ABA* becomes more intense for both the amplitude and the frequency. After we obtain the history of acceleration, we do a fast fourier transform using Matlab code to illustrate the *ABA* response in the frequency domain, which is shown in Fig. 10. At different running speeds, the *ABA* frequency has three main frequencies: 100 Hz, 600 Hz and 1500 Hz. The frequency range with a vibration frequency of about 600 Hz increases significantly with the increase of the running speed. When the speed is above 300 km/h, the higher frequency (1500 Hz) domain is quickly enhanced, and becomes the dominant frequency.

It can be concluded that, the *ABA* is more sensitive to the running speed, while the response of the contact force has a similar shape

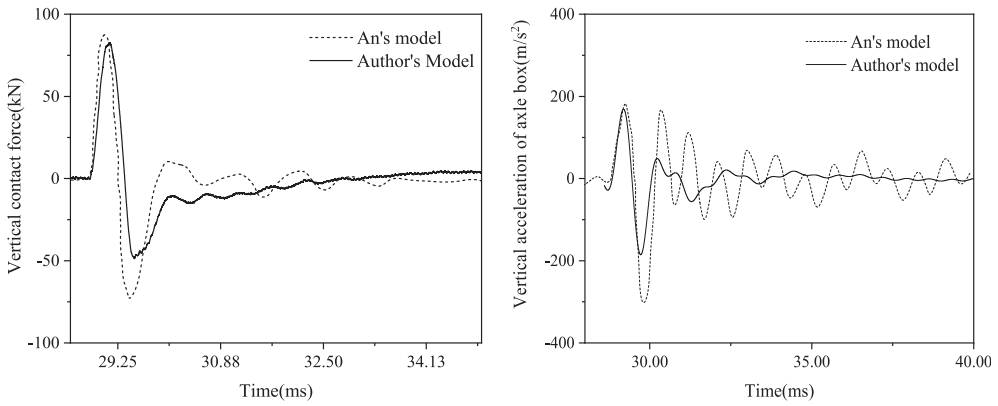

(a) Comparison of contact force (b) Comparison of acceleration

Fig. 6. Verification of the present method.

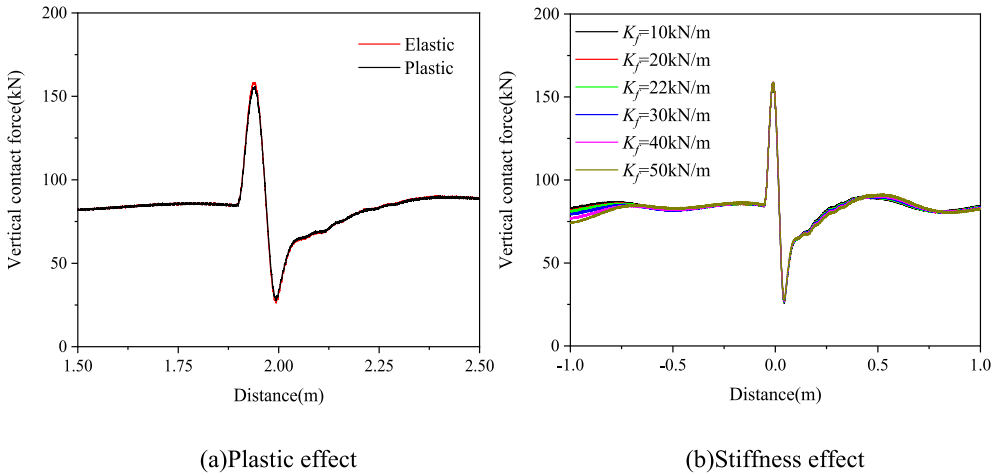

Fig. 7. Plasticity and fastener stiffness effect on contact force.

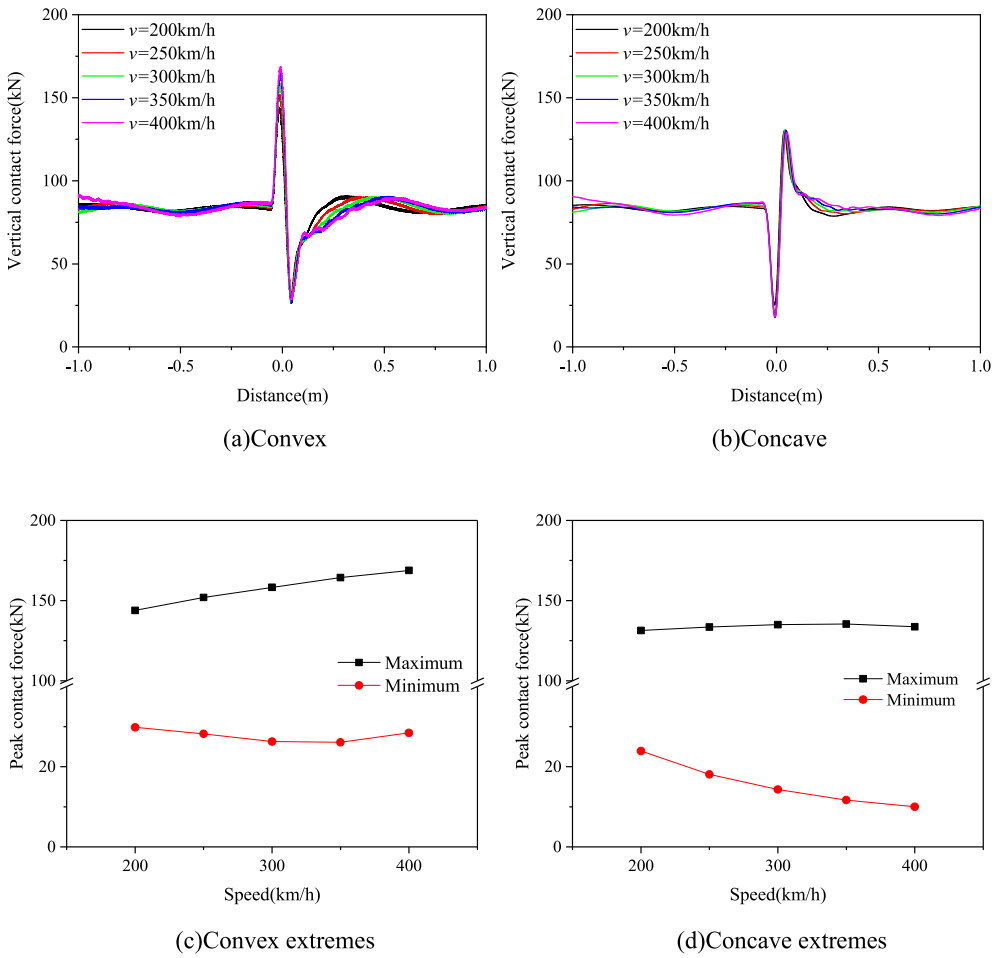

Fig. 8. Comparison of wheel–rail contact force response for different running speeds.

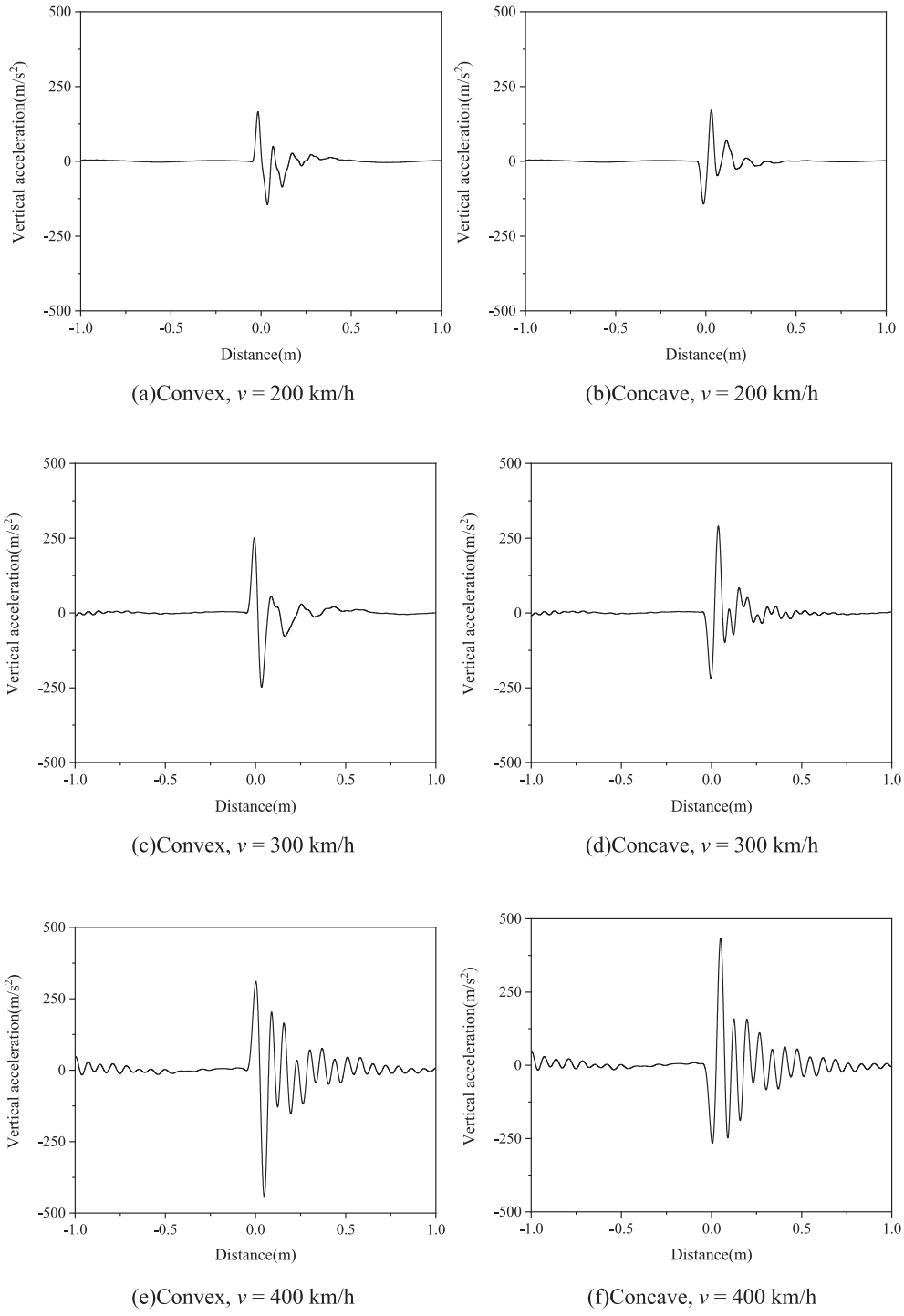

Fig. 9. Vertical acceleration of axle box at different speeds through welded joints.

for all speeds. Compared to the tracking contact force, the monitoring of the *ABA* is a more effective way to determine the operation status of a high–speed train passing the weld.

4.2. The influence of the weld geometry

Wavelength

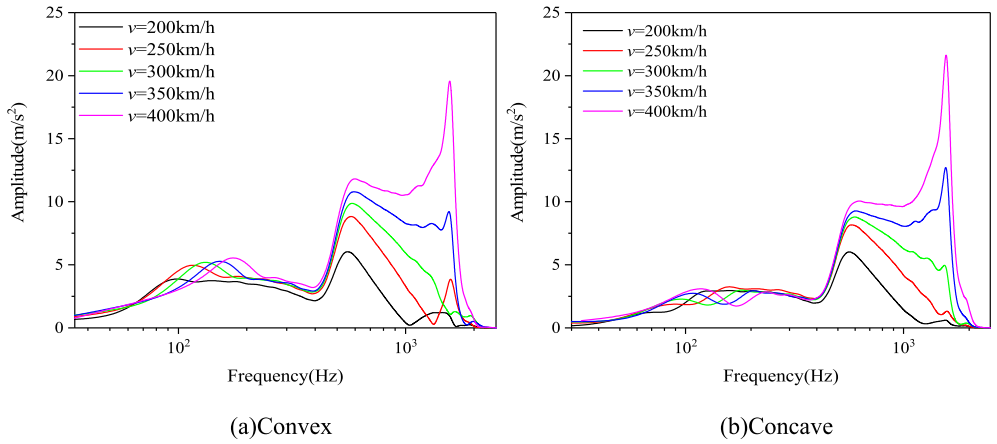

Fig. 10. Vertical acceleration spectrum of axle box at different speeds through welded joints.

This section describes how the wavelength of the weld is varied to check its effect on the wheel–rail contact response. The speed of China's high-speed train is around 300 km/h, and the grinding limit of the weld is 0.2 mm. Thus, in the simulation, the speed is set to be 300 km/h, while the height of the convex weld is chosen as a constant value of 0.2 mm. The specific working conditions are listed in Table. 2.

The results are shown in Table. 3, it indicates that as the wavelength increases 50% (from 0.1 m to 0.15 m), the peak of the contact force changes by less than 6%, but the *ABA* is much more sensitive, and its variation is around 30%–40%. It is suggested that the contact force is not a proper indicator for the variation of the weld wavelength, and the *ABA* should be chosen instead.

Wave height

The height of the convex weld is the main factor affecting the wheel–rail interaction. The grinding limit for a weld is 0.2 mm. Therefore, as described in this section, the wave height is varied from 0.1 mm to 0.3 mm to study the wheel–rail response at the running speed of 300 km/h. The specific working conditions are shown in Table. 4.

Fig. 11 (a) shows the variation of the wheel–rail contact response with different weld heights at a running speed of 300 km/h. It can be seen that, as the wave height of the weld increases, the contact force and the acceleration have a similar history form, but their maximum values increase linearly, as shown in Fig. 12 and Fig. 13. The linearity for the maximum contact force as a function of the wave height is almost the same at different speeds from 200 km/h to 400 km/h. However, the linearity of the acceleration for the wave height is velocity dependent, and the dependence is more obvious at high speed.

The acceleration data is also analyzed in the frequency domain, as shown in Fig. 14. A similar shape of the *ABA* spectrogram can be found for different running speeds. There are three main frequencies. The first frequency is around 100 Hz in the low frequency range, another is around 600 Hz, and the last is around 1500 Hz in the high–frequency range. It is obvious that at the same running speed, the higher value of the wave height produces a wider frequency band. At the lower speed (200 km/h, 300 km/h), the weld generates an acceleration response with a main frequency range of approximately 600 Hz. At the higher speed (400 km/h), an acceleration response with a high–frequency range of approximately 1500 Hz is excited. It can be concluded that the *ABA* spectrogram is very sensitive to the weld height, and it shows an obviously different behavior at a higher speed (400 km/h). These features can be used for detecting the height of the weld.

4.3. Unsymmetric configuration of weld

In the high–speed railway system of China, the geometries of two–sided welds are not always the same. The unsymmetric configuration of weld is studied in this section. this is divided into three cases as described below:

(a) One side with a convex defect, and the other side smooth.
(b) One side with a concave defect, and the other side smooth.
(c) One side with a concave defect, and the other with a convex defect.

Table 2
Working conditions for studying the wavelength of the weld joint.

Welded Geometry	δ (mm)	+0.2					
	λ (m)	0.1	0.11	0.12	0.13	0.14	0.15
Fastener stiffness	K_f (kN/m)	22					
Running speed	v (km/h)	300					

Table 3
Peak responses with different wavelengths.

λ (m)	0.1	0.11	0.12	0.13	0.14	0.15
Maximum vertical contact force(kN)	158.22	156.42	153.92	151.19	149.45	147.02
Maximum upward acceleration(m/s^2)	250.67	233.61	216.91	200.91	186.34	172.25
Maximum downward acceleration(m/s^2)	248.06	197.95	160.06	158.21	154.94	147.85

Table 4
Working condition to study the influence of weld height.

Welded Geometry	δ (mm)	0.1	0.15	0.2	0.25	0.3
	λ (m)	0.1				
Fastener stiffness	K_f (kN/m)	22				
Running speed	v (km/h)	300				

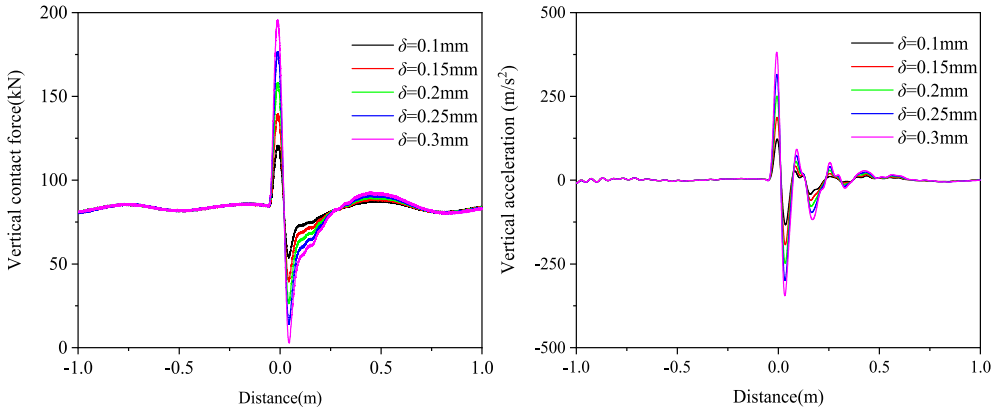

(a) Contact force response, v=300 km/h (b) *ABA* response, v=300 km/h

Fig. 11. Wheel–rail contact responses at welded joints with different wave heights.

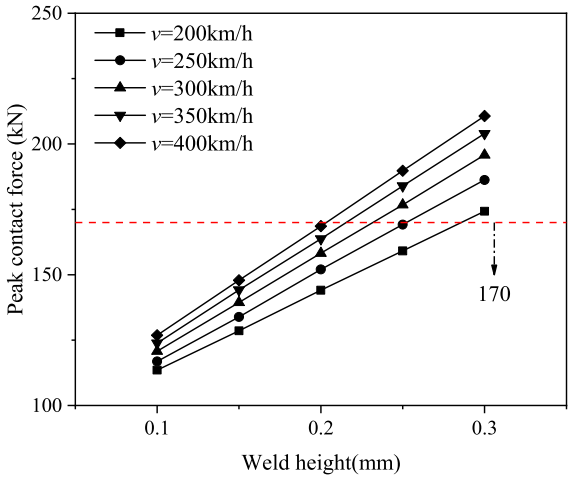

Fig. 12. Maximum value of vertical contact force as a function of the wave height (the dashed line shows the safety limit).

The parameters of various working conditions are given in the Table. 5. To make a comparative analysis, both sides with the same weld configuration are referred to as the routine conditions, i.e.:

Concave routine: Both sides have the same concave defects;

Convex routine: Both sides have the same convex defects.

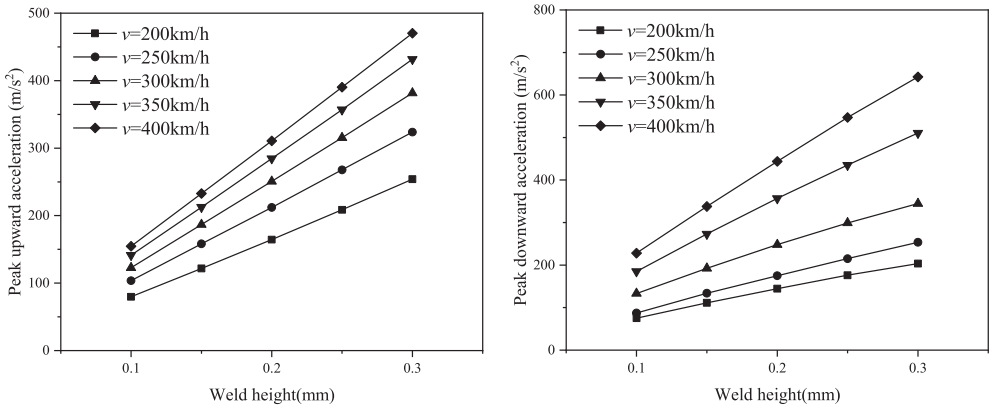

(a)Maximum upward acceleration (b)Maximum downward acceleration

Fig. 13. Variation of the *ABA* as a function of the wave height.

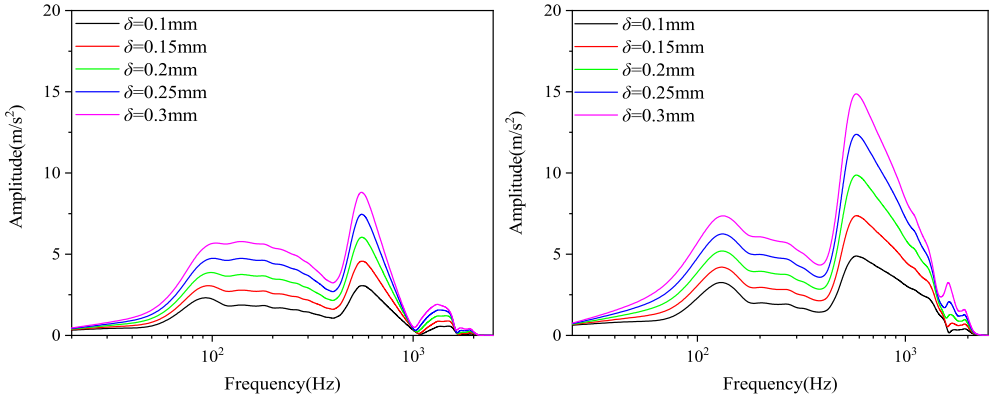

(a) v = 200km/h (b) v = 300km/h

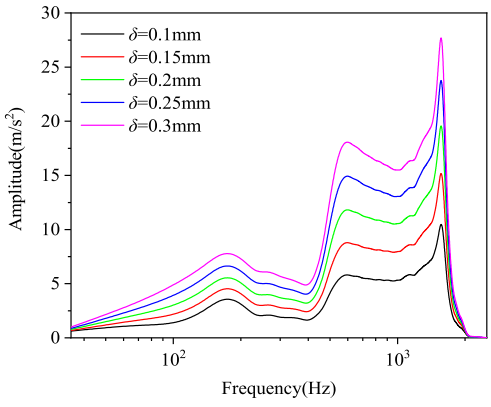

(b) v = 400km/h

Fig. 14. Spectrogram of *ABA* with change of weld height.

As can be seen from Fig. 15. for the one-sided defect system (concave or convex), the contact force of smooth side stays almost unchanged, but the *ABA* shows a different response. It is obvious that, as show in Fig. 15 (a), the *ABA* on the defect side is more severe than that on the smooth side, and the acceleration response from the smooth side is slightly delayed compared to from that on the defect side. The delay is because of the propagation of the dynamic signal from the defect side along the axle. It is interesting to observe

Table 5
Working condition setting for studying on the unsymmetric welds.

Weld geometry	δ (mm)	Left	0.2	−0.2	0.2
		Right	0	0	−0.2
	λ (m)		0.1		
Fastener stiffness	K_f (kN/m)		22		
Running speed	v (km/h)		300		

that, as shown in the spectrogram analysis in Fig. 15 (c) (d). the *ABA* spectrogram for both cases with a one-side weld shows two dominant frequencies. These are a low–frequency band around 150 Hz and a high–frequency band of approximately 600 Hz. The frequency shift of the *ABA* spectrogram for the defect side is not obvious, compared to the routine condition. The frequency shift is obvious for the smooth side, especially the high frequency band (600 Hz), which is shifted to the low frequency regime (500 Hz).

For the case with different defects (one side has a concave defect, and the other has a convex defect), Fig. 16 shows the responses of the wheel–rail contact force and the *ABA*. It can be seen that in this case, the wheel–rail contact forces on the left and right sides are almost symmetrical along the reference line of the axis weight, but the *ABA* vibrations on the left and right sides are not symmetrical. The vibration frequency of the convex side shown in the figure has three main frequencies of vibration, 200 Hz, 600 Hz and 1300 Hz. The main difference, compared with the routine conditions, is that the frequency of the *ABA* has an extra prominent region at a high–frequency (1300 Hz), and the range of the covered frequency band is slightly wider. The *ABA* on the concave side is similar, with a larger response at a high frequency (1300 Hz). The maximum wheel–rail contact force and the *ABA* generated by the above three conditions are given in Table. 6. It is suggested that the difference in the *ABA* between the two sides is much more sensitive than the contact forces to the configurations of the weld. Thus, the *ABA* signal can be used to decide the weld status for the unsymmetric case.

4.4. Safety limit of running speed

Convex routine cases with a wavelength $\lambda = 0.1$ m are discussed below, because this is the most practical condition in the practical situation. Simulations are carried out with varied weld heights. The critical speed as a function of the weld height can be derived, as shown in Fig. 17, based on China's safety limit for the wheel–rail contact force (170 kN as shown in Fig. 12). The critical speed can then be fitted by using:

$$\frac{v}{v_0} = 2.06 \times \left(\frac{\delta}{\delta_0}\right)^{-2.07}$$

δ represents the wave height of the weld, v is the running speed of the train, and δ_0 and v_0 are China's weld reference weld height and train speed. These values are 0.2 mm and 200 km/h, respectively. The running speed should be less than the critical value v with a specific weld height δ.

It is obvious that the monitoring of the *ABA* is much more practical than the measurement of the wheel–rail contact force. From the above analysis for convex routine cases, it is found that the *ABA* is more sensitive to the track irregularity than the wheel–rail contact force. It is therefore useful to discuss the *ABA* safety limits at different running speeds. The dependence of the maximum wheel–rail contact force on the maximum *ABA* is shown in Fig. 18 is obvious that the dependence of the maximum contact force on the maximum upward *ABA* falls on a master line, while the dependence of the maximum contact forces on the maximum downward *ABA* diverges. Thus, it can be concluded that maximum upward *ABA* can be used as the safety limit for a convex weld; its value is approximately 220 m/s^2 to 280 m/s^2 based on China's safety limit for wheel–rail contact force.

5. Limitation of present work

In our model, the weld joint is on one of the sleepers, while in the rail system, the weld might also locate along the span between two sleepers. Previous study [7] showed that the position change has an influence on the maximum contact force, this influence has not been studied in this work. Also, the imposed stress by the thermal contribution [29] has not been considered in present work. In our future work, we will carry out the validation of our model against the experimental on–line test.

Another type of defect, the wheel polygon wear, may induce the *ABA* as high as hundreds of g. This fact also limits the application of the *ABA* for detecting the weld defect. To compare the influences of the wheel polygon wear and the track irregularity on the vibration performance of the wheelset-gearbox system, authors [30] carried out the 1:1 high-frequency excitation test based on the rolling test rig within the speeds of 100 km/h – 500 km/h. Their study [30] concluded that the axle-box acceleration induced by the wheel polygon (48%) is much more than the value by the track irregularity (25%). In our study, we focus on the *ABA* induced by the weld irregularity. In the real test, we only use the acceleration data on the wheel which did not have the polygon wear, because the acceleration signals by the wheel polygon wear and the weld irregularity can be easily separated in the spectrum domain. In another word, if the wheel has a polygon wear shape, we will not use its *ABA*.

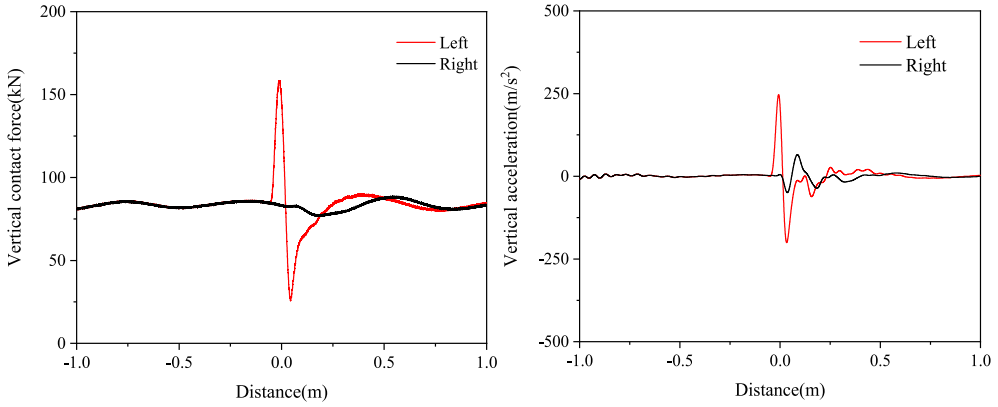

(a) Left side convex, right side smooth

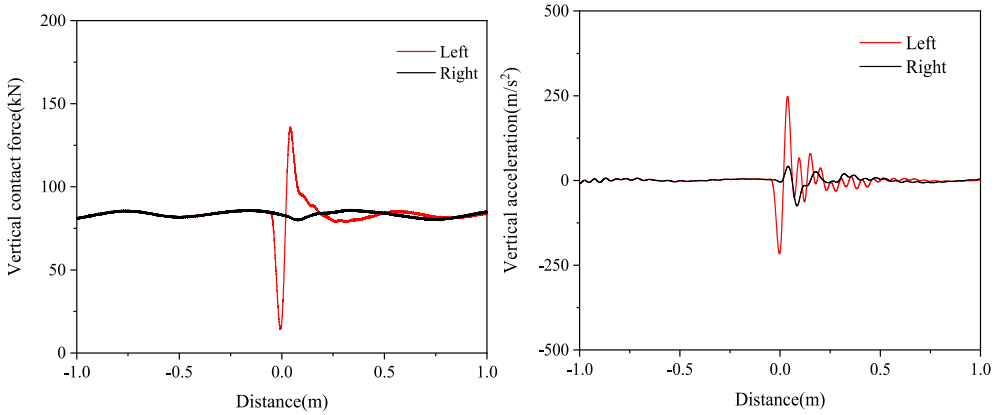

(b) Left side concave, right side smooth

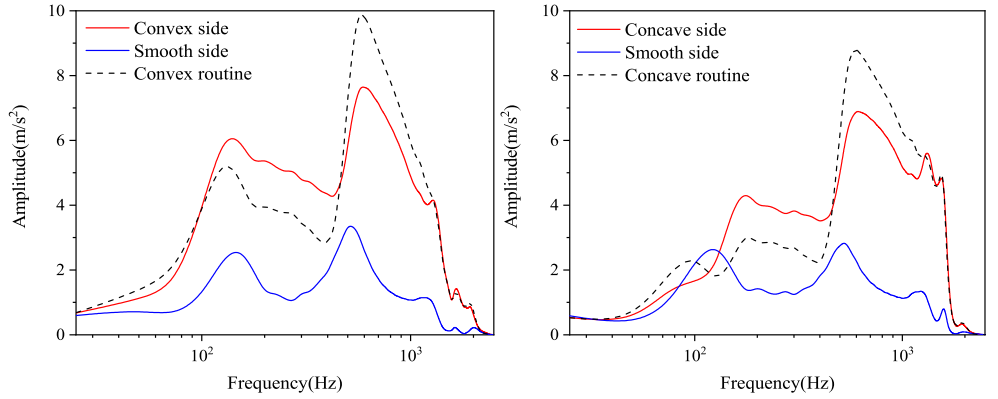

(c) *ABA* Spectrogram for one-side convex (d) *ABA* Spectrogram for one-side concave

Fig. 15. The contact force and *ABA* response of one-side weld case.

6. Conclusion

The wheel–rail dynamic response of passing the weld is simulated by using the finite element method. The conclusions are as follows:

1) For most popular cases in the practical situation with the wave–length $\lambda = 0.1$ m, the critical speed v with a specific weld height δ can be determined by using $v/v_0 = 2.06 \times (\delta/\delta_0)^{-2.07}$.

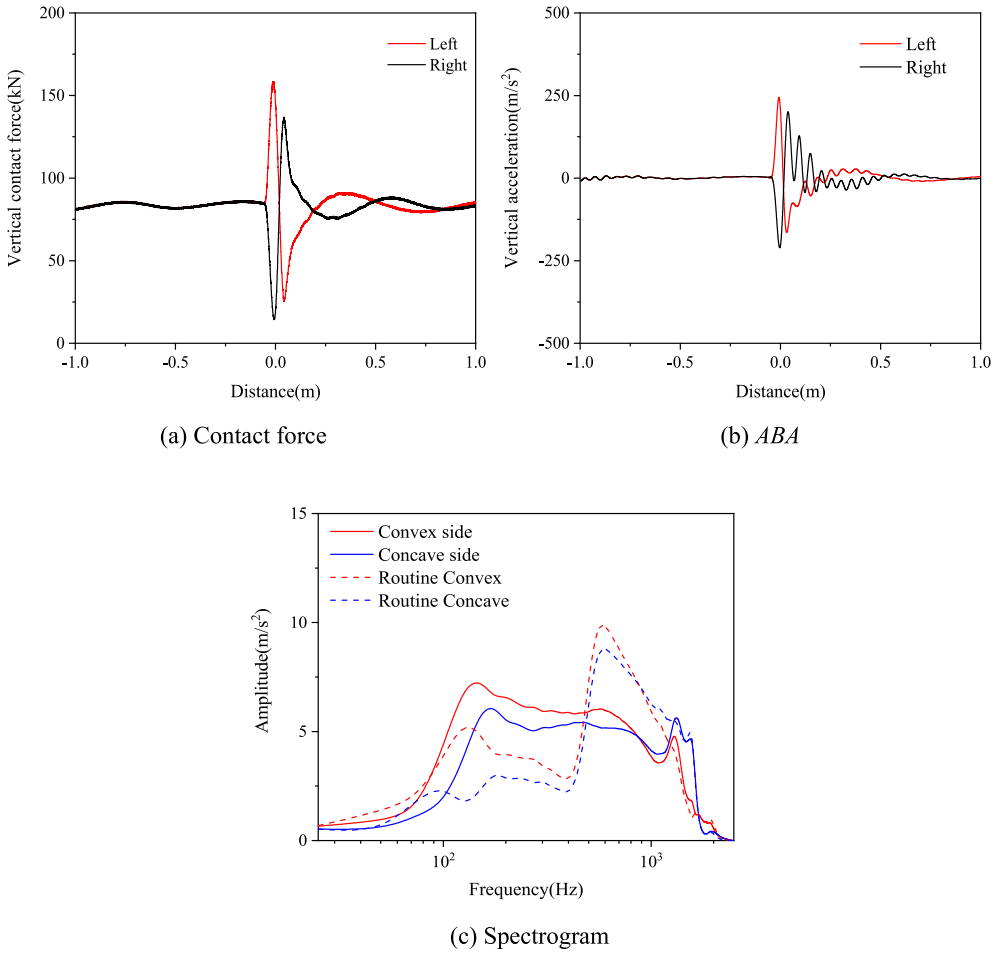

Fig. 16. Wheel–rail contact response with inconsistent weld on both sides.

Table 6
Responses of unsymmetric weld with running speed of 300 km/h.

Working condition		Maximum vertical contact force (kN)	Maximum upward acceleration (m/s^2)	Maximum downward acceleration (m/s^2)
One-side welded	One-side convex	158.27	245.52	196.63
	One-side concave	135.96	248.10	216.44
Two-side different welded	Convex side	158.24	243.87	200.31
	Concave side	136.76	164.28	210.52
Routine	Both-side convex	158.22	250.67	247.46
	Both-side concave	130.71	290.58	220.07

2) The fastener stiffness only affects the low-frequency vibration of the wheel–rail response. As the running speed increases, the vertical contact force of the wheel–rail and the *ABA* peak increase significantly, and the impact vibration of these two parameters rapidly develops to the high frequency band. Therefore, different rail weld defect grinding standards should be set for different running speeds.
3) The increase of the weld wave–length decreases the peak value of the wheel–rail impact response, and the increase of the weld wave height increases the wheel–rail impact response rapidly. The vibration response *ABA* caused by the concave weld is more severe.
4) When there is a defective weld on one side of the rail, the vertical contact force response of the wheel–rail on the smooth side is not large, but the *ABA* response is affected by the defect side and has a more severe response. When there are different weld defects on

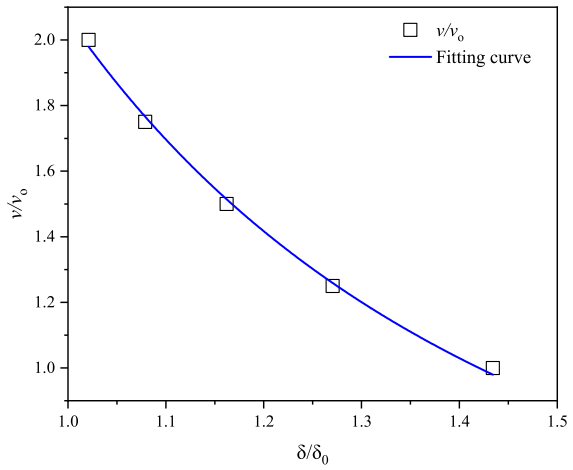

Fig. 17. Critical speed as a function of the weld wave height.

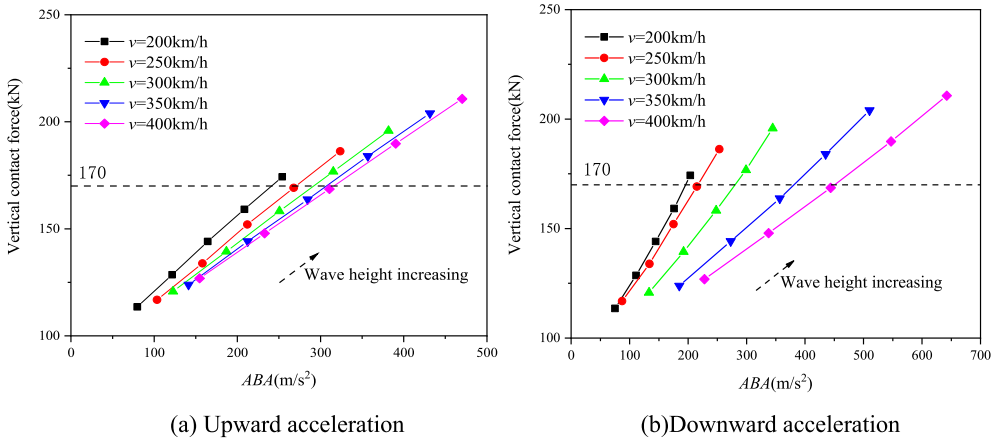

Fig. 18. *ABA* safety limit.

both sides of the rail, the wheel–rail force response on the left and right sides is similar to the normal working condition, but the extreme value of the *ABA* response decreases, especially on the defect side.

5) By using the safety limits for the vertical contact force of a wheel–rail in China, the safety limits of the convex weld and the *ABA* under different running speeds are provided. The acceleration limits 280 m/s^2 and 300 m/s^2, and only the upward acceleration can be used as the monitoring parameter of train operation.

Declaration of Competing Interest

The authors declare that they have no known competing financial interests or personal relationships that could have appeared to influence the work reported in this paper.

Data availability

No data was used for the research described in the article.

Acknowledgement

This work was supported by the National Natural Science Foundation of China (No. 12022210 and 12032001), the Youth Innovation Promotion Association CAS (2018022), and by Foundation of China Academy of Railway Sciences Corporation Limited (2019YJ153). The authors report there are no competing interests to declare.

References

[1] N.H. Lim, N.H. Park, Y.J. Kang, Stability of continuous welded rail track, Comput. Struct. 81 (22–23) (2003) 2219–2236.
[2] P.J. Mutton, E.F. Alvarez, Failure modes in aluminothermic rail welds under high axle load conditions, Eng. Fail. Anal. 11 (2) (2004) 151–166.
[3] P.J. Webster, G. Mills, X.D. Wang, et al., Residual stresses in aluminothermic welded rails, J. Strain Analy. Eng. Des. 32 (6) (1997) 389–400.
[4] A. Skyttebol, B.L. Josefson, J.W. Ringsberg, Fatigue crack growth in a welded rail under the influence of residual stresses, Eng. Fract. Mech. 72 (2) (2005) 271–285.
[5] J. Gao, W. Zhai, Dynamic effect and safety limits of rail weld irregularity on high-speed railways, Scientia Sinica(Technologica) 44 (7) (2014) 697.
[6] M.J.M.M. Steenbergen, C. Esveld, Relation between the geometry of rail welds and the dynamic wheel - rail response: Numerical simulations for measured welds, Proc. Inst. Mech. Eng., Part F: J. Rail Rapid Transit 220 (4) (2006) 409–423.
[7] N. Correa, E.G. Vadillo, et al., On the non-proportionality between wheel/rail contact forces and speed during wheelset passage over specific welds, J. Sound Vibration. 413 (2018) 79–100.
[8] J.J. Kalker, K.L. Johnson, Three-Dimensional Elastic Bodies in Rolling Contact, Kluwer Academic Pub, 1990.
[9] W. Zhai, C. Cai, S. Guo, Coupling Model of Vertical and Lateral Vehicle/Track Interactions, Veh. Syst. Dyn. 26 (1) (1996) 19.
[10] M.J.M.M. Steenbergen, C. Esveld, Rail weld geometry and assessment concepts, Proc. Inst. Mech. Eng., Part F: J. Rail Rapid Transit 220 (3) (2006) 257–271.
[11] R. Dong, Vertical dynamics of railway vehicle-track system. PhD thesis, Concordia University, Canada, 1994.
[12] X. Zhao, Z.L. Li, The solution of frictional wheel–rail rolling contact with a 3D transient finite element model: Validation and error analysis, Wear 271 (2011) 444–452.
[13] Z.L. Wei, Z.L. Li, Z.W. Qian, R. Chen, R. Dollevoet, 3D FE modelling and validation of frictional contact with partial slip in compression-shift-rolling evolution, Int J Rail Transp 4 (2016) 20–36.
[14] X. Zhao, Z. Li, A solution of transient rolling contact with velocity dependent friction by the explicit finite element method, Eng Comput 33 (2016) 1033–1050.
[15] Z. Yang, Z.L. Li, R. Dollevoet, Modelling of non-steady-state transition from single-point to two-point rolling contact, Tribol Int 101 (2016) 152–163.
[16] Z.F. Wen, X.S. Jin, W.H. Zhang, Contact-impact stress analysis of rail joint region using the dynamic finite element method, Wear 258 (2005) 1301–1309.
[17] W. Cai, Z.F. Wen, X.S. Jin, W.M. Zhai, Dynamic stress analysis of rail joint with height difference defect using finite element method, Eng Fail Anal 14 (2007) 1488–1499.
[18] Y.C. Chen, J.H. Kuang, Contact stress variations near the insulated rail joints, Proc. Inst. Mech. Eng. Part F J. Rail Rapid Transit 216 (216) (2002) 265–273.
[19] E. Kabo, J.C.O. Nielsen, A. Ekberg, Prediction of dynamic train-track interaction and subsequent material deterioration in the presence of insulated rail joints, Veh. Syst. Dyn. 44 (sup1) (2006) 718–729.
[20] B. An, P. Wang, J. Xiao, J. Xu, R. Chen, Dynamic Response of Wheel-Rail Interaction at Rail Weld in High-Speed Railway, Shock Vib. 2017 (2017) 1–11.
[21] M. Molodova, Z. Li, R.P.B.J. Dollevoet, Axle box acceleration: Measurement and simulation for detection of short track defects, Wear 271 (1) (2011) 349–356.
[22] S.C. Sun, Theoretical Research on Wheel/Rail Contact Force Identification and Its Application, China Academy of Railway Sciences, Beijing, 2016.
[23] C. Chang, C. Wang, Y. Jin, Study on numerical method to predict wheel/rail profile evolution due to wear, Wear 269 (3–4) (2010) 167–173.
[24] M. Yu, Transient simulation for high-speed track/vehicle system and study on rail corrugation, China Academy of Railway Sciences, Beijing, 2019.
[25] M. Yu, W.D. Wang, J.Z. Liu, et al., The transient response of high-speed wheel/rail rolling contact on “roaring rails” corrugation, Proc. Inst. Mech. Eng. Part F J. Rail Rapid Transit 233 (10) (2019) 1068–1080.
[26] K. Koro, K. Abe, M. Ishida, et al., Timoshenko beam finite element for vehicle—track vibration analysis and its application to jointed railway track, Proc. Inst. Mech. Eng. Part F J. Rail Rapid Transit 218 (2) (2004) 159–172.
[27] Z. Wen, G. Xiao, X. Xiao, X. Jin, M. Zhu, Dynamic vehicle–track interaction and plastic deformation of rail at rail welds, Eng. Fail. Anal. 16 (2009) 1221–1237.
[28] Rules for maintenance of high-speed railway lines, China National Railway Group, 2012.
[29] I. Grossoni, P. Shackleton, Y. Bezin, et al., Longitudinal rail weld geometry control and assessment criteria, Eng. Fail. Anal. 80 (2017) 352–367.
[30] P. Liu, S. Yang, Y. Liu, Full-scale test and numerical simulation of wheelset-gear box vibration excited by wheel polygon wear and track irregularity, Mech. Syst. Sig. Process. 167 (2022), 108515.